

Validation study of the magnetically self-consistent inner magnetosphere model RAM-SCB

Yiqun Yu,¹ Vania Jordanova,¹ Sorin Zaharia,¹ Josef Koller,¹ Jichun Zhang,² and Lynn M. Kistler²

Received 31 October 2011; revised 16 December 2011; accepted 27 January 2012; published 17 March 2012.

[1] The validation of the magnetically self-consistent inner magnetospheric model RAM-SCB developed at Los Alamos National Laboratory is presented here. The model consists of two codes: a kinetic ring current–atmosphere interaction model (RAM) and a 3-D equilibrium magnetic field code (SCB). The validation is conducted by simulating two magnetic storm events and then comparing the model results against a variety of satellite in situ observations, including the magnetic field from Cluster and Polar spacecraft, ion differential flux from the Cluster/CODIF (Composition and Distribution Function) analyzer, and the ground-based SYM-H index. The model prediction of the magnetic field is in good agreement with observations, which indicates the model’s capability of representing well the inner magnetospheric field configuration. This provides confidence for the RAM-SCB model to be utilized for field line and drift shell tracing, which are needed in radiation belt studies. While the SYM-H index, which reflects the total ring current energy content, is generally reasonably reproduced by the model using the Weimer electric field model, the modeled ion differential flux clearly depends on the electric field strength, local time, and magnetic activity level. A self-consistent electric field approach may be needed to improve the model performance in this regard.

Citation: Yu, Y., V. Jordanova, S. Zaharia, J. Koller, J. Zhang, and L. M. Kistler (2012), Validation study of the magnetically self-consistent inner magnetosphere model RAM-SCB, *J. Geophys. Res.*, 117, A03222, doi:10.1029/2011JA017321.

1. Introduction

[2] The inner magnetosphere is a complex and dynamically coupled system of various plasma populations overlapping with each other. This domain covers the closed field-line region near the Earth, mainly from the dayside magnetopause to the middle plasma sheet on the nightside. A ring current is generated when the charged particles move separately due to the gradient-curvature drift in a nonuniform magnetic field environment. This current system carries 10–200 keV energy particles and varies significantly during magnetic active times when plasma is accelerated by the tail reconnection toward the Earth and energized adiabatically when it moves into the stronger field region close to the Earth. The freshly injected ions convect toward the dayside through the dusk side, generating a partial ring current. The ring current carries a large fraction of the total particle energy of the inner magnetosphere and thus substantially influences the overall magnetic configuration. The plasmasphere, surrounding the Earth, is comprised of low energy particles, with their origin mainly

from the ionosphere. This population does not directly affect the magnetic configuration, but contains most of the mass of the magnetosphere and can affect the wave-particle interactions which are very important in understanding the sources and losses from the ring current as well as the radiation belt [Lyons *et al.*, 1972; Millan *et al.*, 2002]. The radiation belts are a population with MeV energetic charged particles. These energetic MeV particles can also undergo dramatic changes during storm times [Reeves *et al.*, 2003], such as a dropout of relativistic electron flux. What causes these changes and how the particles are transported and accelerated are still actively debated scientific topics. These three plasma populations overlap with each other, complicating the physical processes and hence the theoretical modeling of the near-Earth space environment.

[3] With reasonable assumptions and boundary setups, researchers have made a lot of progress on modeling the inner magnetosphere dynamics. Due to the wide energy range in different particle populations and differential drift of charged particles, the ring current is generally represented well by models that solve the kinetic equation describing the motion of keV-energy ions and electrons:

$$\frac{\partial f}{\partial t} + \mathbf{v} \cdot \frac{\partial f}{\partial \mathbf{r}} + \mathbf{a} \cdot \frac{\partial f}{\partial \mathbf{v}} = \left(\frac{\delta f}{\delta t} \right)_{\text{loss}} + \left(\frac{\delta f}{\delta t} \right)_{\text{diffusion}} \quad (1)$$

where \mathbf{v} , \mathbf{a} , and f are velocity vector, acceleration vector, and distribution function, respectively. Different kinetic models

¹Space Science and Application, Los Alamos National Laboratory, Los Alamos, New Mexico, USA.

²Space Science Center, University of New Hampshire, Durham, New Hampshire, USA.

interpret this distribution function in different ways. For example, the Rice Convection Model (RCM) describes the adiabatically drifting particle distribution by a number of “fluids” in a self-consistently computed electric field, assuming the distributions are isotropic. This model relies on external feed of magnetic fields that are needed to drive the convection of the particles. It can also be coupled to the Magneto-Friction code that computes the 3-D equilibrium magnetic field [Lemon *et al.*, 2004; Yang *et al.*, 2011] and is therefore referred to as the RCM-E model. The distribution function f in the RCM or RCM-E model is interpreted as the number of particles per magnetic flux volume [Wolf, 1983; Toffoletto *et al.*, 2003]. Another inner magnetosphere model, the Comprehensive Ring Current Model (CRCM) describes f as the phase space density of a particle species $f(\mu, J)$ [Fok *et al.*, 2001], where μ is the magnetic moment and J is the second adiabatic invariant. A third model, the Ring Current-Atmosphere Interactions Model (RAM) [Jordanova *et al.*, 1996, 1997, 2006], which we use in this study, considers f as the phase space density $Q(E, \mu_o)$, where E is the kinetic energy of particles, and μ_o is $\cos(\alpha_o)$ where α_o is the equatorial pitch angle. A detailed description of RAM is provided in section 2.

[4] With various models developed to represent inner magnetospheric dynamics, one important step before further delivering the model to the community for acceptance and wide usage is to validate the model output versus observations. This study will investigate the performance of the ring current model RAM self-consistently coupled with a magnetic field model [Zaharia *et al.*, 2004, 2006; Zaharia, 2008], which is also described below. This validation work will present the model capability of reproducing actual magnetic storm events and show how the model results depend on the model’s external driving parameters such as the electric field.

2. Model Description

[5] The inner magnetosphere model RAM-SCB is composed of two fully coupled codes: the kinetic ring current-atmosphere interactions model (RAM) and the 3-D equilibrium magnetic field code (SCB). The RAM model [Jordanova *et al.*, 1994, 2006] numerically solves the bounce-averaged kinetic equation for the distribution functions for the ring current ions H^+ , O^+ , and He^+ and electrons. The distribution function $Q_l(R_o, \phi, E, \mu_o, t)$ is evaluated in the magnetic equatorial plane from 2 to $6.5 R_E$ for all magnetic longitudes ϕ , kinetic energy E of the particles from 0.1 keV to 400 keV, and pitch angle α_o ($\mu_o = \cos(\alpha_o)$) from 0 to 90° :

$$\begin{aligned} & \frac{\partial Q_l}{\partial t} + \frac{1}{R_o^2} \frac{\partial}{\partial R_o} \left(R_o^2 \left\langle \frac{dR_o}{dt} \right\rangle Q_l \right) + \frac{\partial}{\partial \phi} \left(\left\langle \frac{d\phi}{dt} \right\rangle Q_l \right) \\ & + \frac{1}{\gamma p} \frac{\partial}{\partial E} \left(\gamma p \left\langle \frac{dE}{dt} \right\rangle Q_l \right) + \frac{1}{h\mu_o} \frac{\partial}{\partial \mu_o} \left(h\mu_o \left\langle \frac{d\mu_o}{dt} \right\rangle Q_l \right) \\ & = \left\langle \left(\frac{\partial Q_l}{\partial t} \right)_{\text{loss}} \right\rangle \end{aligned} \quad (2)$$

The angle brackets represent bounce averaging, the subscript index o denotes the equatorial plane. p is the

relativistic momentum of the particle, γ is the relativistic factor, and h is defined by

$$h(\mu_o) = \frac{1}{2R_o} \int_{s_m}^{s'_m} \frac{ds}{\sqrt{(1 - B(s)/B_m)}} \quad (3)$$

which is proportional to the bounce period, being the so-called “half-bounce path length” [e.g., Roederer, 1970], normalized by $1/2R_o$. Here, B_m is the magnetic field at the mirror point, ds is distance interval along the integrating field line, and R_o is the equatorial distance of the field line.

[6] In the RAM computational domain (i.e., the equatorial plane from 2 to $6.5 R_E$), the grid resolution is $0.25 R_E$ in the radial direction and 15° in the azimuthal direction in the SM coordinate system. At the nightside boundary (i.e., $6.5 R_E$), the plasma inflow flux is determined by the energetic particle flux measurements from the Magnetospheric Plasma Analyzer (MPA) and the Synchronous Orbit Particle Analyzer (SOPA) on board LANL geosynchronous satellites, after interpolating the data over the gaps in the magnetic local times. To serve as the boundary condition, the inflow flux needs to be decoupled into individual plasma compositions, which can be done by employing the empirical function developed by Young *et al.* [1982], who correlated the plasma sheet ion composition with solar and magnetospheric conditions.

[7] The right hand side of equation (2) represents loss processes of charged particles as they move around the Earth; in this paper we include the collisions with the dense upper-atmosphere and charge exchange with neutral hydrogen (see Jordanova *et al.* [2010] for details). The left hand side of the equation describes acceleration and transport motions of charged particles along their adiabatic drift paths. The transport of the particles is mainly governed by the gradient-curvature drift and convective drift, which are controlled by the time-dependent convection electric field and magnetic field. The convection electric field in the RAM model can be specified either by a semi-empirical convection model, the Volland-Stern model [Volland, 1973; Stern, 1975; Maynard and Chen, 1975], or by an empirical ionospheric potential model, Weimer01 [Weimer, 2001]. The ionospheric potential is mapped from the ionosphere down to the magnetic equator along magnetic field lines, obtaining the convective electric field in the equatorial plane as a function of radius and local time.

[8] The magnetic field in the RAM model, needed in the bounce-average integrals as well as to drive the particle transport, is no longer a dipolar field as before but rather updated every 5 min by the 3-D equilibrium code SCB. The SCB model numerically solves the single-fluid plasma force-balance equation $\mathbf{J} \times \mathbf{B} = \nabla \cdot \mathbf{P}$ where \mathbf{P} is the pressure tensor, and \mathbf{J} is the current density. The anisotropic pressure calculated from the moments of the RAM distribution function serves as input to the SCB code every 5 min. The anisotropic pressure along the magnetic field lines is obtained after mapping from the equatorial plane by applying the Liouville’s theorem [Zaharia *et al.*, 2006; Liemohn, 2003]. With anisotropic pressure, the right hand side of the force-balance equation can be expressed as

$$\nabla \cdot \mathbf{P} = \nabla P_\perp - \nabla \cdot [(P_\perp - P_\parallel)\mathbf{bb}] \quad (4)$$

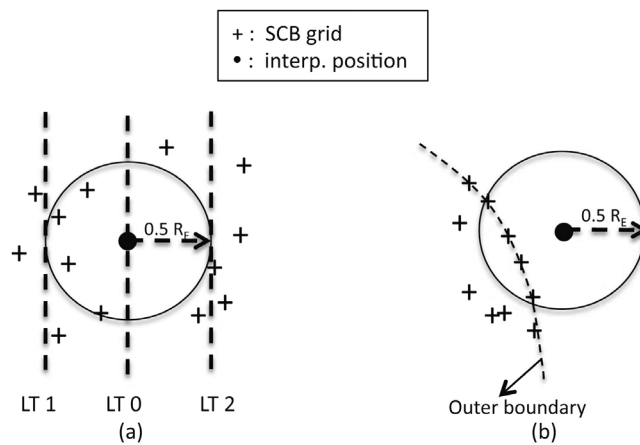


Figure 1. Schematic illustration of two problems using the Kd tree method and subsequently the nearest neighbor interpolation. Figure 1a shows that the four nearest neighbors (enclosed by the sphere) are from the same-side local time with respect to the interpolation location. Figure 1b shows that the four neighbors come from the outer boundary when the interpolation position is above the boundary. These two cases violate the spirit of “interpolation” by not fully surrounding the interpolation location.

where P_{\parallel} and P_{\perp} represent the parallel and perpendicular pressure, respectively, and \mathbf{b} is the unit vector of the magnetic field. The force-balance equation is actually solved in flux coordinate (Euler potential) space by expressing the magnetic field as $\mathbf{B} = \nabla\alpha \times \nabla\beta$, where α and β are Euler potentials. The magnetic field lines are formed by the intersection of constant α and β surfaces. After numerically solving the Euler potential equations, the magnetic field is obtained in the SM coordinate system and the field-geometric integrals $h(\mu)$ (equation (3)) and $I(\mu_o) = 1/R_0 \int_{s_m}^{s_m'} \sqrt{(1 - B(s)/B_m)} ds$, which is related to the second adiabatic invariant, are computed and fed back to the ring current model. These integrals can be easily computed inside the SCB code as they are integrated over one dimension. Besides the anisotropic pressure input, the SCB code also requires the Euler potential α boundary conditions on the inner and outer magnetic flux surfaces that confine the SCB computation domain. The value of Euler potential α and the shape of the surfaces is determined in this work by the Tsyganenko 89 model [Tsyganenko, 1989] after field tracing. Since T89 model is parameterized by the time-dependent Kp index, the shape of the computation domain is therefore changing in time. The Euler potential β on the boundary is periodic in the azimuthal direction.

3. Data Description

[9] The in situ satellite measurements used to compare against the model results in this validation study include the magnetic field observed by Cluster/FGM [Balogh *et al.*, 2001] and Polar/MFE [Russell *et al.*, 1995] instruments, and the energy differential ion flux obtained from Cluster/CODIF (Composition and Distribution Function) analyzer

[Rème *et al.*, 2001]. The Polar satellite has a highly elliptical polar orbit with the apogee/perigee of $9/1.8 R_E$ and a period of 18 hours. Cluster, a four spacecraft mission, has a polar orbit with an apogee of $19.6 R_E$ and perigee of $4 R_E$ and a period of 57 hours.

[10] The CODIF sensor in the CIS (Cluster Ion Spectrometer) instrument on board the Cluster spacecraft determines the energy and directional distribution of major ion species H^+ , He^+ , He^{++} , and O^+ over an energy range from 15 eV/e to 40 keV/e. The instrument is a combination of a top cap electrostatic analyzer followed by a post acceleration of 15 kV and a time-of-flight measurement. One problem associated with the measurement is that, while the energetic populations are hardly affected, the lower energy composition data can be significantly contaminated under intense radiation belt conditions when the satellite is closer to the Earth (i.e., near a perigee pass). As the RAM-SCB model covers the inner magnetosphere region, the satellite trajectory, along which the differential flux is to be compared, is inside this domain and is therefore usually close to the Earth ($<6.5 R_E$), where the data in the lower energy band is likely to be contaminated. In the following comparisons with the ion differential flux from CODIF, the low energy composition data is thus recovered by a background subtraction technique. Such a technique removes the background contamination by subtracting a background contamination level and can most of the time recover the main spectral features of the lower energy populations.

4. Modeled Magnetic Field and Ion Differential Flux

[11] By flying a satellite inside the 3-D computation domain of SCB, the magnetic field at a particular satellite location is obtained after interpolating the magnetic field values from nearby grids. Since the 3-D equilibrium code solves for the Euler potentials and then magnetic field in the Euler potential coordinates (α, β, χ) (where χ is a coordinate along the field line), the grids, viewed from regular Cartesian or spherical coordinates, are irregular. Two different interpolation methods have thereby been implemented in the code to first build up a global mesh structure and then interpolate to Cartesian: (1) k-d tree construction and nearest neighbor interpolation, and (2) Delaunay triangulation and natural neighbor interpolation.

[12] To find the neighboring grid points for the field interpolation, the k-d tree [Bentley, 1980], which is a space-partitioning data structure to organize data points in k dimensional space, is utilized to create a tree-type structure from over 100,000 grid points. Such a tree provides good efficiency in searching for the nearest neighbors for the subsequent interpolation, saving significant computing time. The nearest neighbors are restricted inside a sphere centered at the interpolation position with a radius of $0.5 R_E$, outside of which the grids are not taken into account. If no neighbors are found inside this sphere, the interpolation position is considered to be outside the computation domain, thereby returning no information on the magnetic field. The subsequent interpolation from the neighbors is done by weighting the individual field vectors from the neighbors, with the weight being the inverse of the distance away from the interpolation location. However, such a nearest neighbor

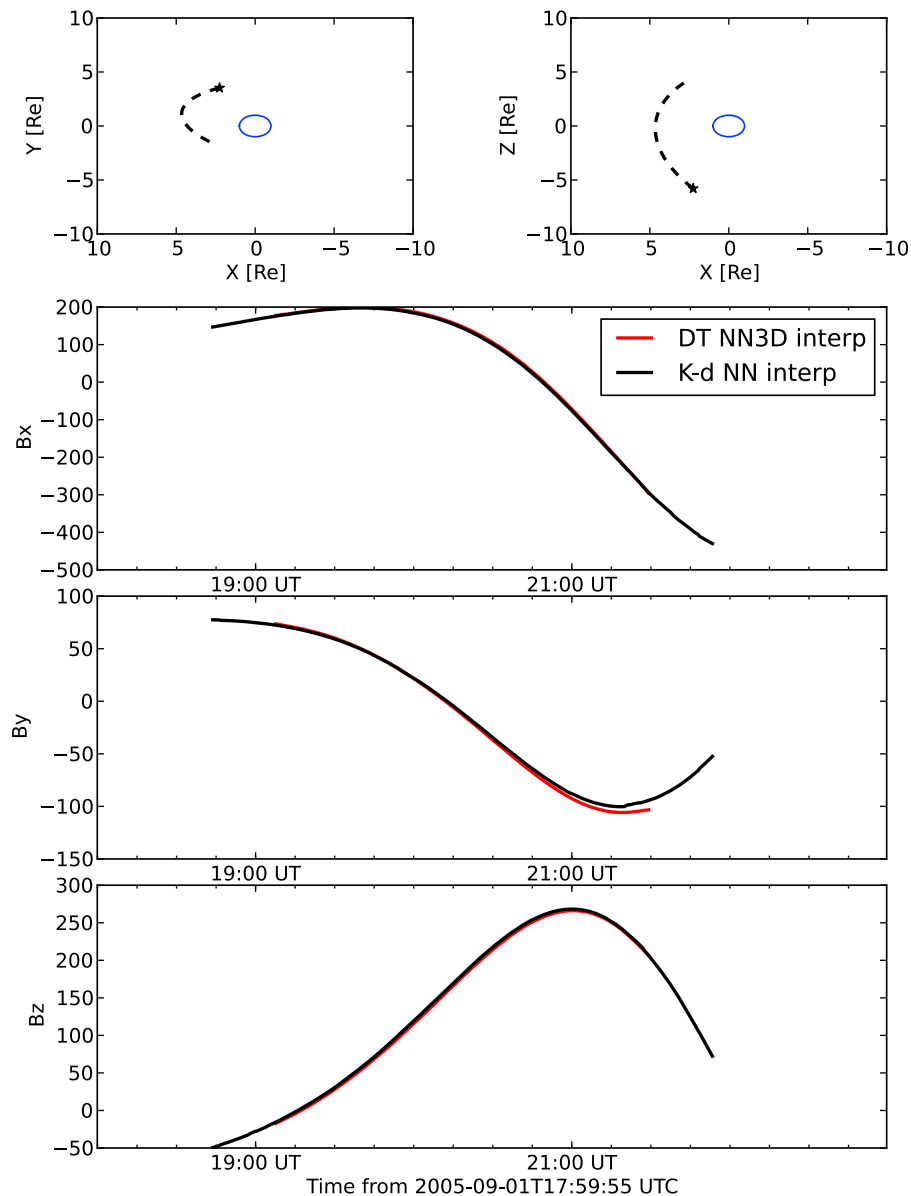


Figure 2. For a Cluster trajectory flying through the RAM-SCB computation domain, the magnetic field vector is interpolated using two different methods: Delaunay triangulation + natural neighbor interpolation (red) and K-d tree + nearest neighbor interpolation (black). Both the location and magnetic field vector are in SM coordinates. The unit of magnetic field is nT. The red curve (using the Delaunay triangulation and natural neighbor interpolation method) is shorter because no interpolation is done outside the outer boundary of the model’s computation domain (Delaunay triangulation is only performed inside the “convex hull”) even though the interpolation location is very closely outside the boundary.

searching and the associated interpolation might sometimes cause problems. For example, all of the resulting neighbors could come from the same side local times with respect to the local time where the point of interest resides (Figure 1a). In other words, the to-be-interpolated point is not “surrounded” by its nearest neighbors. This clearly deviates from the desired nature of “interpolation.” It can happen as well when the point of interest is outside the outer boundary (Figure 1b), with all the grid points beneath it, although they are still inside the $0.5 R_E$ sphere.

[13] The natural neighbor interpolation [Sibson, 1981] is popular for its more smooth approximation and more precise

interpolated results than the nearest neighbor interpolation. It is based on Voronoi tessellation and Delaunay triangulation of a set of spatial points. The weights used for the interpolation between the neighbors are the overlapped volume between the Voronoi cell associated with the interpolation location relative to the natural neighbor data and the Voronoi cell associated with the same natural neighbors in the absence of the interpolation point. However, building the Delaunay triangulation and computing the Voronoi polygon tessellation among 10^6 3-D grid points are tremendously slow.

[14] Figure 2 illustrates the interpolated magnetic field along a Cluster trajectory inside the SCB computation

domain using both methods. Only approximately 3-hour satellite trajectory is resolved by the model, because most of the time the Cluster spacecraft flies outside the model's computation domain. The method with Delaunay Triangulation and natural neighbor interpolation (red line) shows a shorter trajectory since the Voronoi cells formed from the grid points must surround the interpolation location, leaving it unable to deal with any location outside the boundary; while the k-d tree and nearest neighbor interpolation allows limited interpolation locations outside the boundary as long as their distances to the neighbors are less than $0.5 R_E$, resulting in a longer interpolated trajectory. But for the overlapped trajectory well inside the SCB domain, the two methods demonstrate very similar interpolations. Knowing the high computational cost of the creation of the Delaunay triangulation and Voronoi tessellation over 100,000 grid (the lower limit of the SCB grid) points, in the following sections where the simulated magnetic field is presented, the first interpolation method (i.e., k-d tree and nearest neighbor interpolation) is applied due to its much faster speed.

[15] The ion differential flux at any location inside the 3-D model is obtained by first mapping along the field line down to the equatorial plane where the ring current particles distribution function is solved by RAM. Since the differential flux is a function of pitch angle and kinetic energy, and the magnetic moment and the energy are both conserved, the corresponding equatorial pitch angle can be easily calculated through $\sin(\alpha)/B = \text{const}$ where α is the pitch angle and B is the local magnetic field. The equatorial phase space density $Q(\mu_o, E)$ at the mapping position can then be obtained through interpolating from RAM grids. This equatorial phase space density is then mapped along the field lines to the location of interest, since in the bounce-averaged formalism the phase space density is conserved along the bounce path. The mapped phase space density is subsequently converted to the differential flux $f(\alpha, E)$ by $f = Q * p^2$ where p is momentum. In such a way, the ion differential flux along any trajectory inside the 3-D model domain is computed and can be compared with in situ observations.

5. Validation

[16] Two magnetic storm events are selected to perform the model validation: 20 November 2002 storm and 31 August 2005 storm. The interplanetary and magnetospheric conditions for the two events are illustrated in Figure 3. The 20 November 2002 event (Figure 3, left) shows two dips in the SYM-H index, with the minima being -80 nT and -120 nT respectively. The first disturbance is a result of southward turning of the IMF Bz component which then lasts for about 2 hours before it turns to northward orientation again. The second one is associated with a southward turning of IMF Bz, ramp up of the solar wind speed, and large magnetic field in the Y direction. The August storm (Figure 3, right) shows a minimum SYM-H index of -120 nT, and is a result of a shock arriving at the magnetopause which accompanies a sudden southward turning of Bz component lasting for 10 hours and an enhancement of solar wind density. The initial condition for the RAM particle distribution in both events is set up by the measurements taken

from the HYDRA and MICS instruments on board the Polar spacecraft during quiet times.

5.1. Magnetic Storm Event: 20 November 2002

[17] This section compares the simulated magnetic field along Cluster and Polar trajectories and ion differential flux along Cluster trajectory with in situ observations.

[18] Figure 4a shows the modeled SYM-H index and the observed SYM-H index (blue). Two convection electric field models are utilized for comparison: the Weimer 01 model, which uses interplanetary parameters and AL index to obtain the electric potential in the ionosphere, and the Volland-Stern model, which obtains the equatorial electric potential that depends on Kp index and is symmetric about the noon-midnight meridian. The modeled SYM-H indices using these two electric field drivings are illustrated in green and red lines respectively. The modeled SYM-H index is calculated from the Dessler-Parker-Sckopke (DPS) relationship [Dessler and Parker, 1959; Sckopke, 1966], which linearly relates the magnetic field perturbation with the energy content of the ring current E_{RC} :

$$\Delta B[nT] = -B_E \frac{2E_{RC}}{3U_E} = -3.98 \times 10^{-30} E_{RC}[keV] \quad (5)$$

where B_E is the equatorial surface magnetic field strength of the Earth's dipole and U_E is the magnetic energy of the dipole field beyond the Earth surface. This ΔB represents the magnetic field perturbation at the center of the Earth, rather than on the surface as the real SYM-H index is measured. The effect from the induced currents in the Earth and the magnetopause currents, included in the real SYM-H index, is however excluded in this ΔB . Both simulations miss the first dip in the real SYM-H profile, but the simulation using the Weimer electric field model reasonably reproduces the second main phase, although the model tends to create an earlier, more rapid decrease in the profile. However, the modeled SYM-H index using Volland-Stern electric field driving appears to be less intense, implying that the Volland-Stern electric field could not provide strong enough electric field to accelerate and transport the particles into the dust sector inner magnetosphere region, while the Weimer electric field during the second main phase is excessively strong, intensifying the ring current nearly instantly.

[19] In the simulation with the Weimer electric field driving, four snapshots (marked by the vertical lines in the SYM-H plot) are chosen throughout the storm time, corresponding to pre-storm, first dip, second dip, and the recovery phase, respectively. The dial plots display the total pressure (Figure 4b), H^+ flux at ~ 2 keV (Figure 4c), and H^+ flux at ~ 100 keV (Figure 4d) at above four time shots. While a very small partial ring current is seen at the first SYM-H dip, missing the realistic intensity of the ring current that is responsible for the first decrease shown in the measured SYM-H index, a much stronger partial ring current is clearly built up at the third time shot in the dusk sector. The ring current intensification is related to the ring current injection rate that is affected by the variation of the convection potential and the plasma sheet density. Therefore, the increase only in the convection potential and a small change in the plasma sheet density at the first SYM-H dip do

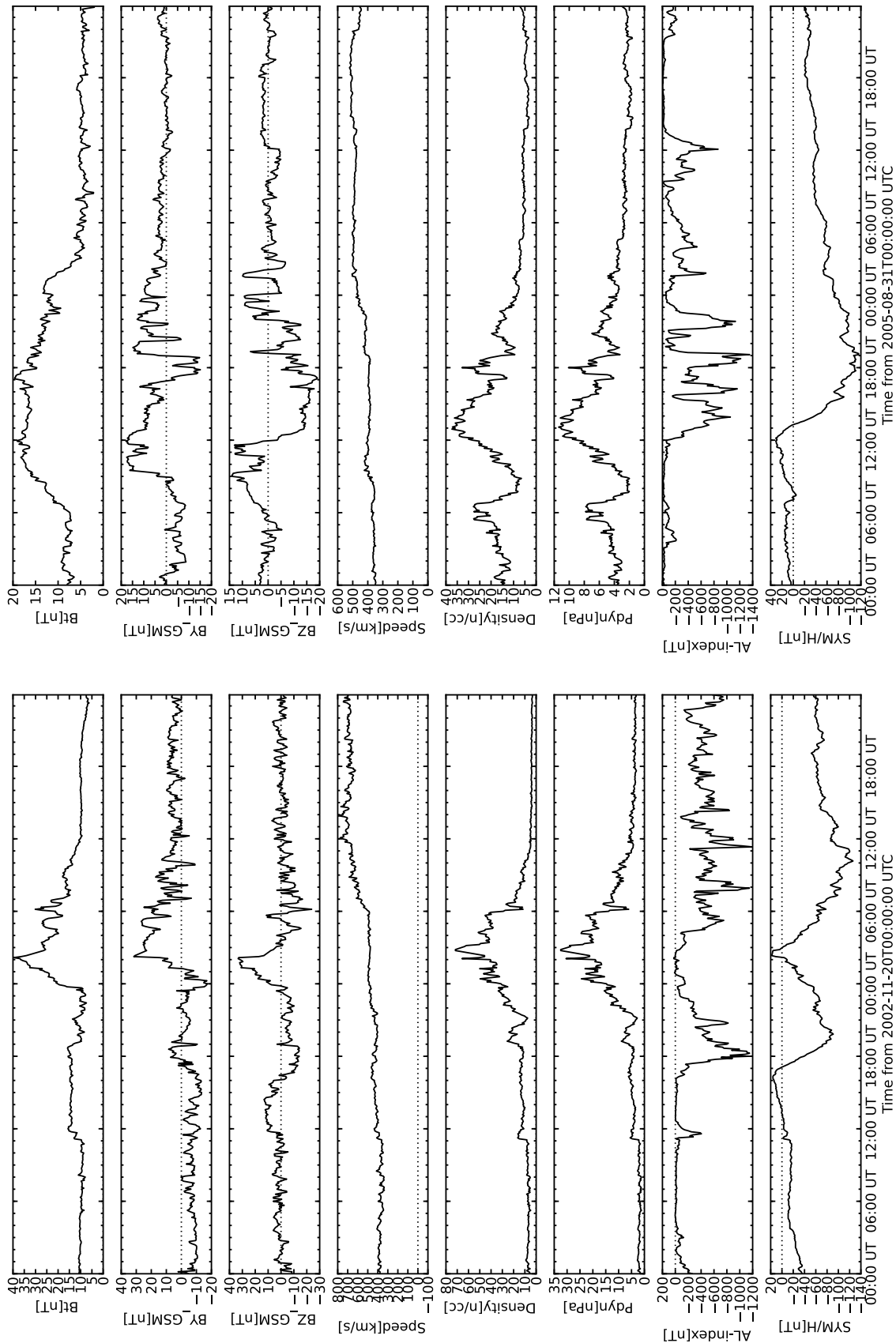


Figure 3. The interplanetary and magnetospheric conditions for two magnetic storm events: (left) 20 November 2002 and (right) 31 August 2005.

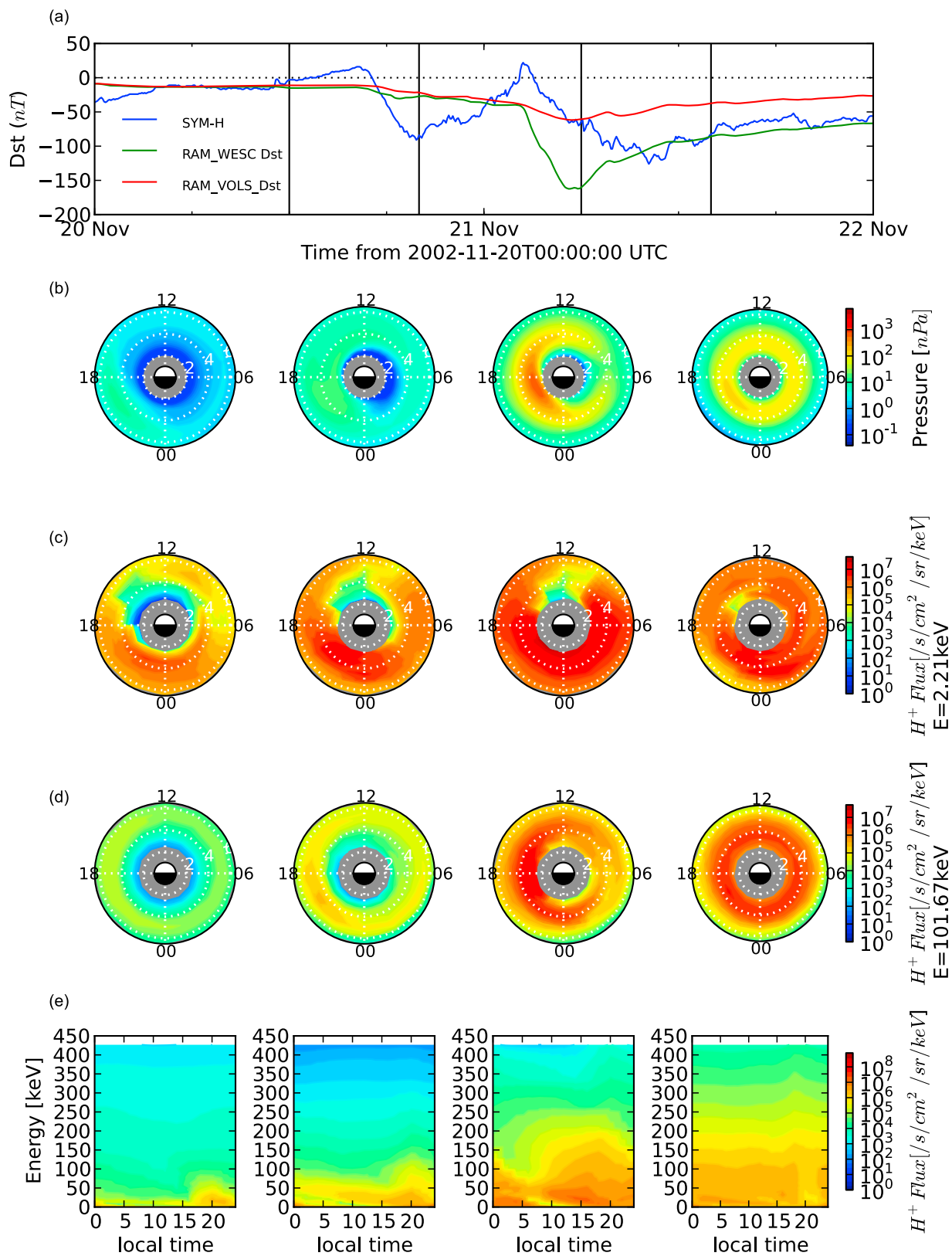


Figure 4. Simulation results for the storm event 20 November 2002. (a) The observed SYM-H index (blue) and the SYM-H index calculated from RAM-SCB model with the Weimer electric field along SCB field lines (WESC, green) and the Volland-Stern electric field (VOLS, red). The remaining plots represent simulation results using the Weimer electric field at four snapshots (time marked by the vertical lines): (b) total pressure, (c) H^+ flux at the energy level of ~ 2 keV, (d) H^+ flux at a higher energy level ~ 100 keV, and (e) energy - LT (local time) contour plots of H^+ flux at $4.0 R_E$.

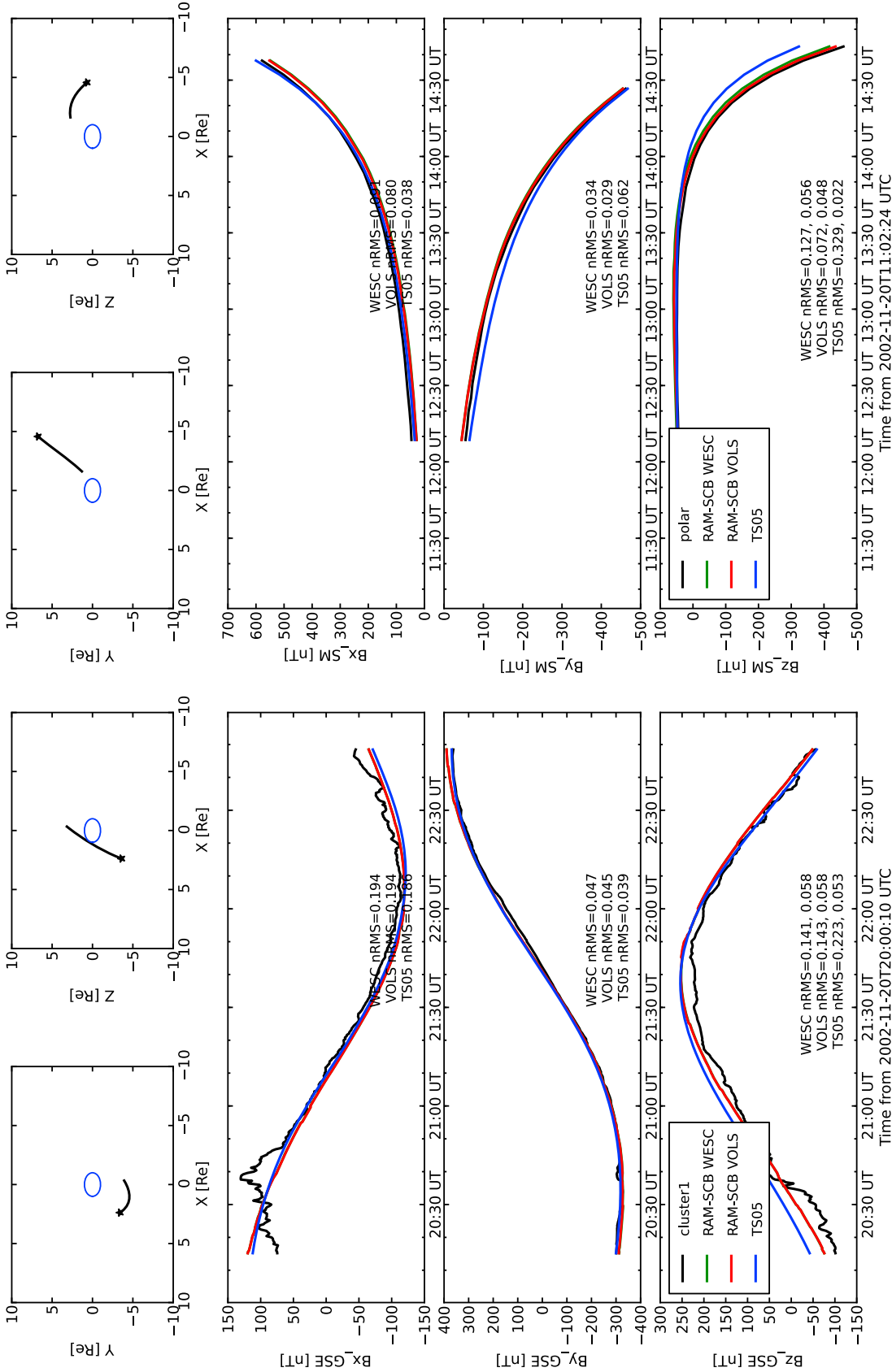
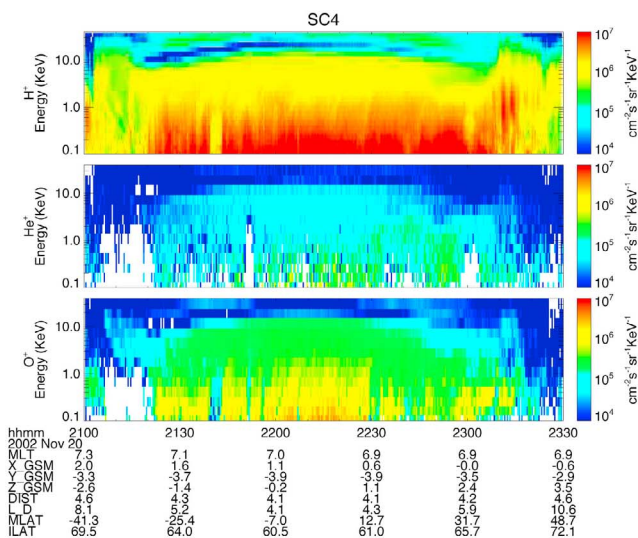
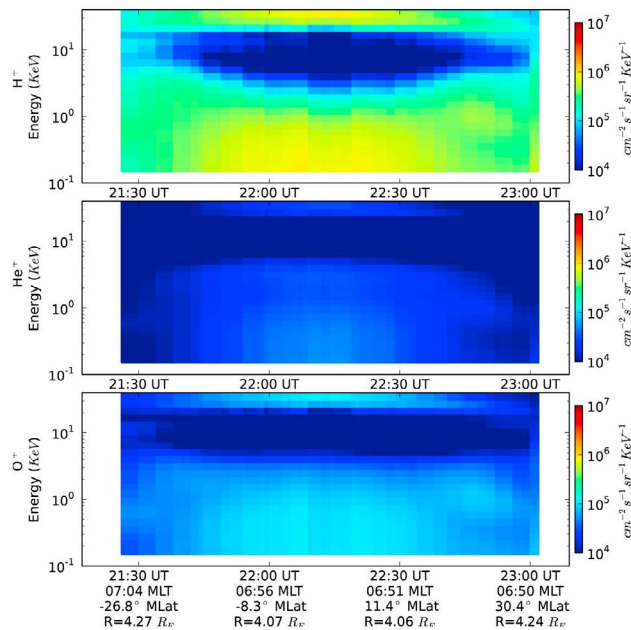


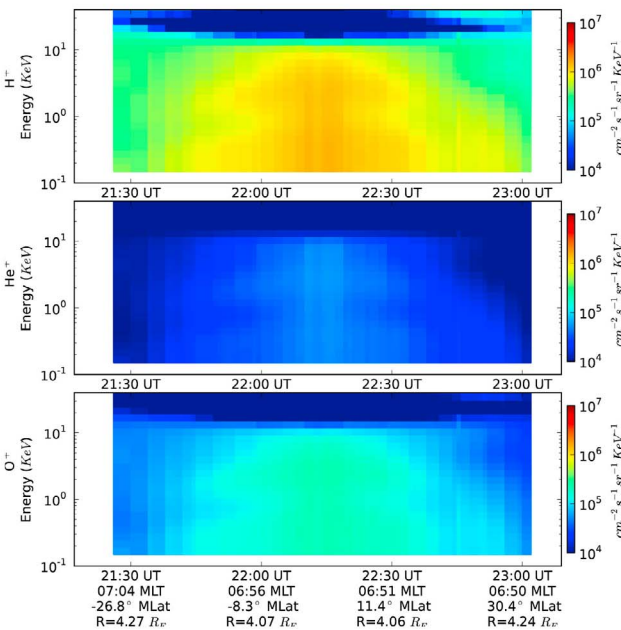
Figure 5. The magnetic field computed by RAM-SCB model using Weimer electric field along SCB field lines (WESC, green) and the Volland-Stern electric field (VOLS, red) for storm event 20 November 2002. The in situ observation (black line) and the field obtained from the Tsyganenko 05 storm model (blue line) are illustrated for comparison. Left plots show magnetic fields along a Cluster trajectory, and right plots show magnetic fields along a Polar trajectory. Note that the green and red lines are nearly overlapped. The trajectories shown are inside the model domain. The numerical values are the normalized RMS errors for each field component and magnitude (bottom right plot), measuring the agreement between the model and observation.



(a) Cluster/CODIF observation



(b) RAM-SCB with Weimer01



(c) RAM-SCB with Volland-Stern

Figure 6. Ion flux spectrograms from (a) Cluster/CODIF measurement, (b) RAM-SCB simulation with the Weimer electric field driving, and (c) RAM-SCB simulation with the Volland-Stern electric field driving during the main phase of storm 20 November 2002 (time starts from 20 November 2002, 21:00 UT in the plots). The flux is pitch angle averaged.

not lead to a large enough ring current injection [Jordanova et al., 2010] and created a weak ring current.

[20] The low energy H^+ flux (Figure 4c) is enhanced starting from midnight and then convects to most local times. The flux intensity decreases slightly in the recovery phase. The high energy flux (Figure 4d) increases less significantly in the dusk sector during the main phase and then fills in all the local times while the intensity fades, but is trapped between the inner boundary and $6 R_E$. Figure 4e

shows energy-LT maps of the H^+ flux at a radial distance of $4 R_E$. The flux clearly increases from the dusk sector toward the dayside, and the high energy flux gradually becomes enhanced at all local times.

5.1.1. Magnetic Field Comparison

[21] The magnetic field interpolated by the k-d tree and nearest neighbor interpolation method along a Cluster trajectory is compared with data, as shown in Figure 5 (left). For the time period when the satellite is inside the model’s

computation domain, the satellite is orbiting on the post-dawn side around $5 R_E$ across the magnetic equator toward the northern hemisphere. The RAM-SCB model using the two different electric field models (in green and red lines; note that they are almost overlapped) reproduces equally well the actual magnetic field except near 20:40 UT. The increase in the observed magnetic field at this time may be related to a field distortion caused by the large ring current injection which causes the first dip in the SYM-H index, while the model misses this injection rate and hence no similar variation is reproduced. To evaluate the agreement between the model and data, the normalized RMS error is utilized:

$$nRMS = \frac{\sqrt{\langle (B_m - B_d)^2 \rangle}}{\sqrt{\langle B_d^2 \rangle}} \quad (6)$$

where B_m is the modeled magnetic field and B_d is the data. The role of nRMS error is to evaluate the agreement by comparing to 1: less than 1 indicates that the model and data are trending together, with little offset between them; zero being the perfect matching with each other; greater than 1 means that the data and the model may possibly have opposite trends or large offsets between them. The overall simulated magnetic field shows a good agreement with the data, with the normalized root-mean square (RMS) error less than 0.2. Also plotted for comparison is the magnetic field computed from the Tsyganenko 2005 (TS05) [Tsyganenko and Sitnov, 2005] empirical model in blue lines, which suggest that the RAM-SCB model performs better in reproducing the B_z component than the empirical model. The magnetitude of the magnetic field from these models shows similar nRMS errors.

[22] The magnetic field measured by the Polar spacecraft (Figure 5, right) is also well captured by the model using either electric field driving when the satellite is flying in the nightside magnetosphere toward the Earth from the equator to the polar region. The normalized RMS errors for the three magnetic field components are also small, less than 0.15. Again, the RAM-SCB model produces better B_z component than the TS05 empirical model. Both magnetic field comparisons with Cluster and Polar measurements indicate that the RAM-SCB model is capable of representing the inner magnetospheric field configuration well, which means that the model is trustworthy in applications that involve field tracing, such as L^* calculation in radiation belt studies [Roederer, 1970] which entirely relies on the accuracy of the global magnetospheric field configuration.

5.1.2. Differential Ion Flux Comparison

[23] The ion differential flux spectrograms from both the RAM-SCB model and the CODIF sensor on board Cluster spacecraft 4 are shown in Figure 6. The flux is pitch angle averaged. The satellite is near the equatorial dawn side during the storm main phase. Both electric field models are used for comparison. Figure 6b shows the ion fluxes using the Weimer potential model, the Figure 6c use the Volland-Stern model, and Figure 6a illustrates the Cluster observations. Only energy levels from 0.1 to 40 keV are shown for the comparison, as they are the overlapped energy range between the model and instrument. With the Weimer convection model, the H^+ flux spectrogram shows an ion flux

gap region around 3–20 keV, which is wider in energy coverage when the spacecraft is near perigee. Such an ion flux gap region and the surrounding flux enhancement are likely to be associated with the “nose structure” [Vallat *et al.*, 2007] which is observed frequently in the inner magnetosphere and is characterized by a flux increase in a narrow energy range. The model O^+ flux also shows a flux “depleted” region in the energy range between 4 and 20 keV. While the data does indicate an H^+ flux gap region, it is much narrower. On the other hand, the O^+ flux observation shows a depleted region above 10 keV, without enhancement at higher energy levels in the available energy range. With the Volland-Stern convection electric field model, the spectral gap regions are narrower and appear around a higher energy level, which is more consistent with the data.

[24] To give an intuitive comparison between the data and model results, fluxes for H^+ , O^+ , and He^+ ions chosen at different times are illustrated in Figure 7 as a function of energy, with both electric field models being employed for comparison. Figure 7 (left) shows ion fluxes at magnetic local time around 7:00 and latitude around -9° , with a radial distance of $4.0 R_E$. The low energy (below 1 keV) H^+ flux is underestimated using either electric field model, but the magnitude of middle-energy flux (1 keV–10 keV) is better predicted and the general trends of the high-energy (>10 keV) flux are better captured by applying the Volland-Stern convection electric field drives and accelerates the plasma in a more correct way than the Weimer electric field model at this particular time. Figure 7 (right) shows ion fluxes at magnetic latitude of 30.4° at a later time. Again, the low energy flux is underestimated using either of the electric field models, and no significant discrepancy in the flux is seen between the two electric field models at this particular time and location.

[25] Figure 8 illustrates the flux along the satellite trajectory at energy levels of 1.0 keV (Figure 8, left) and 10 keV (Figure 8, right). The low energy (1.0 keV) H^+ and O^+ flux in the model are both underestimated by an order of magnitude, while the He^+ flux is reproduced within the noisy range of the observation for most of the time. The high energy (10 keV) flux with Volland-Stern driving electric field is much closer to the observation, while the flux with Weimer electric field driving is significantly smaller than the data.

[26] The above flux observations occur during the first storm main phase, which, however, is not captured by the model using either the Weimer electric potential model or the Volland-Stern model. The observations were taken at post-dawn local times, which are not strongly affected by the enhancement of energy density during a storm main phase that normally happens in the midnight-dusk sector. Around this time and location, the convection potential produced by the Volland-Stern model is larger and penetrates deeper into the magnetosphere than that by the Weimer model, as shown by Jordanova *et al.* [2010, Figure 1 at Hour 22]. This larger electric field transports and accelerates particles to higher energies, resulting in a better prediction of the flux at high energy levels. This implies the necessity and advantage of implementing a self-consistent electric field in the inner magnetosphere model, since the eastward “skewed” electric field can transport low energy ions into the post-midnight sector and peaks the ion flux in the dawn sector [C:son Brandt *et al.*, 2002; Fok *et al.*, 2010]. A self-consistent

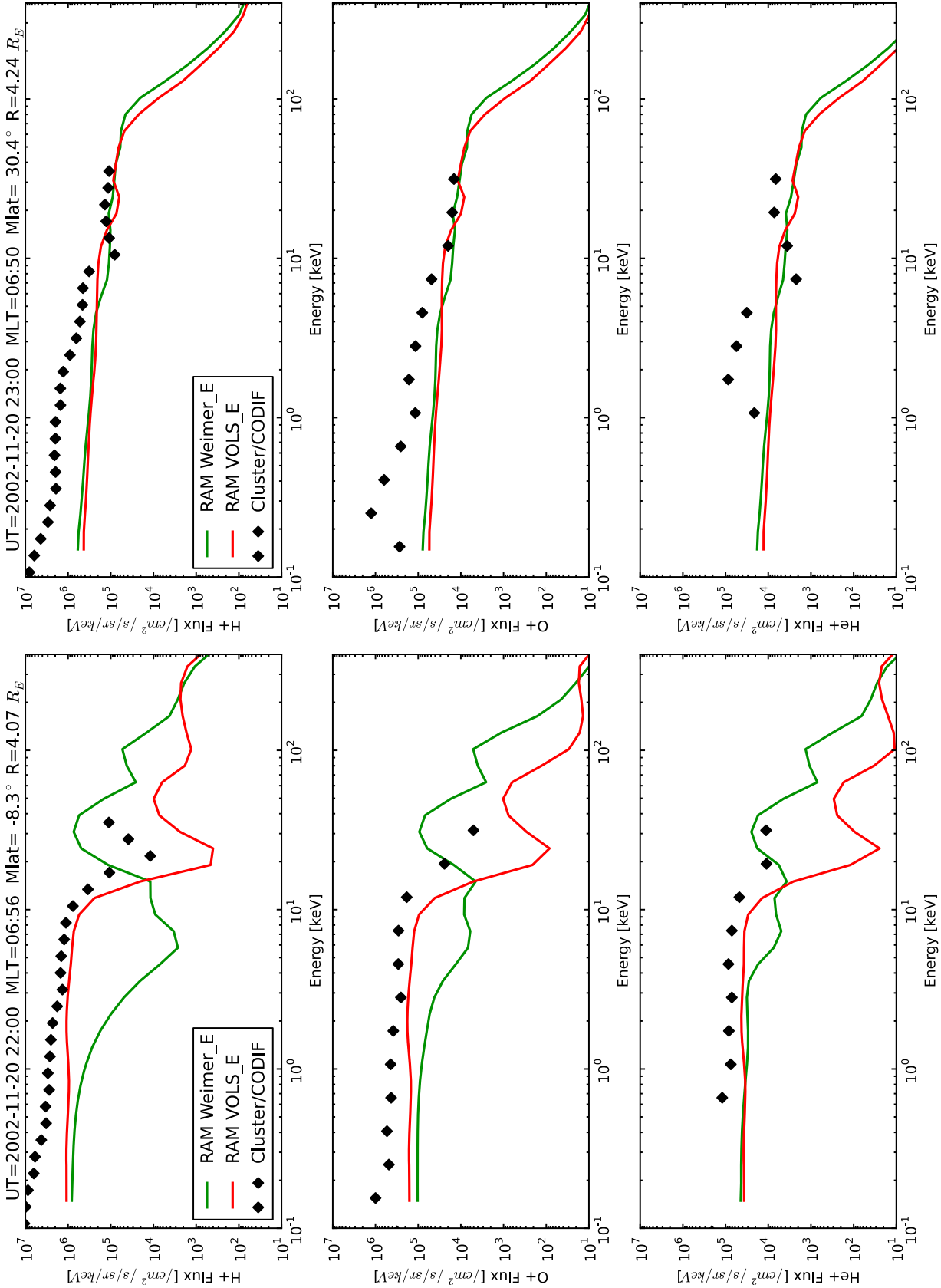


Figure 7. Ion (H^+ , O^+ , He^+) differential flux as a function of energy observed by Cluster/CODIF (diamond) and produced by the model using either Weimer01 (green) or Volland-Stern (red) electric field driving at two different times during the first main phase of the storm 20 November 2002. The flux is pitch angle averaged.

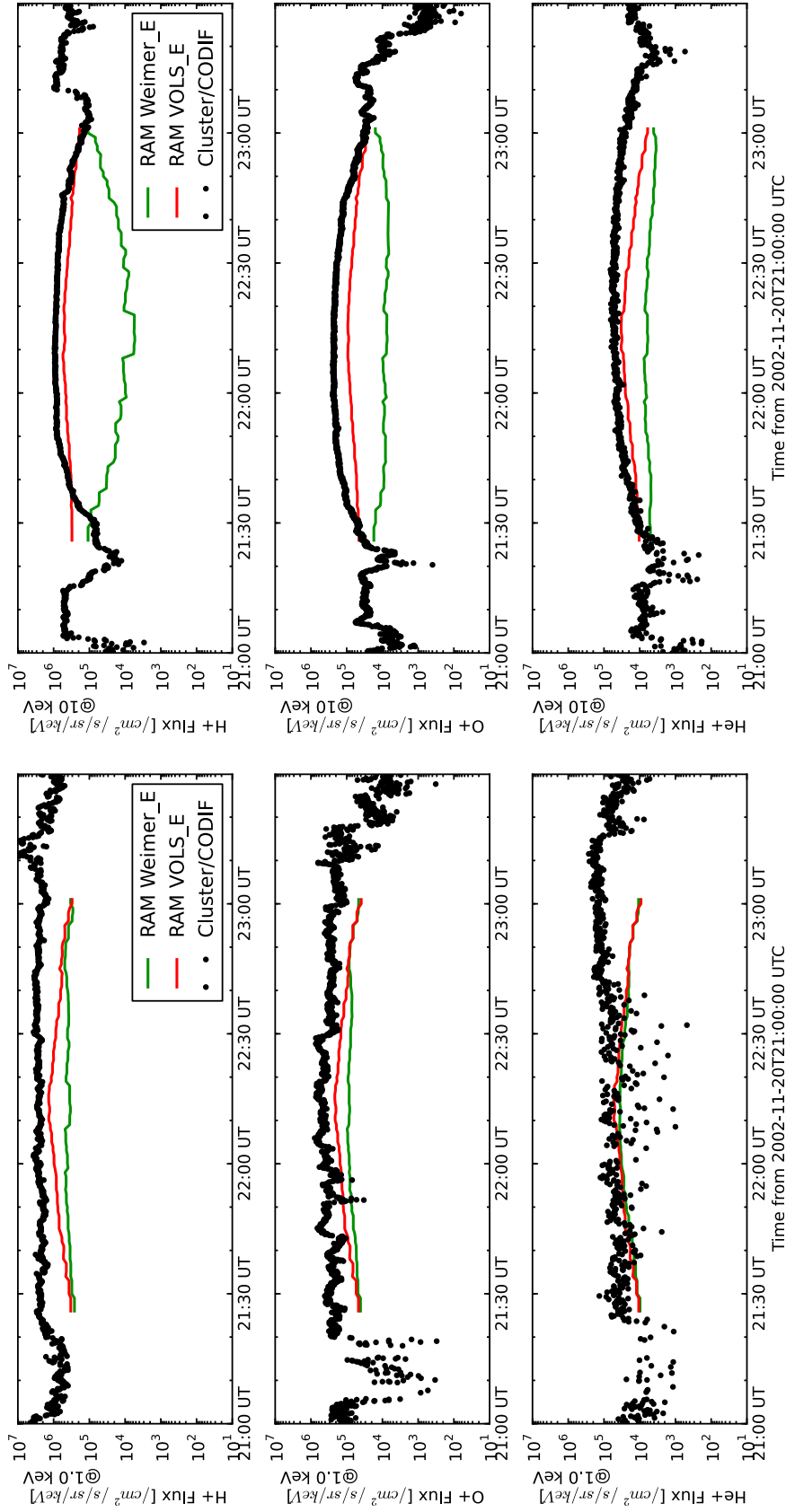


Figure 8. Ion (H^+ , O^+ , He^+) differential flux along the Cluster trajectory observed by Cluster/CODIF (black dots) and produced by the model using either Weimer01 (green) or Volland-Stern (red) electric field driving for two different energy levels: (left) 1 keV and (right) 10 keV, in the storm event 20 November 2002. The flux is pitch angle averaged.

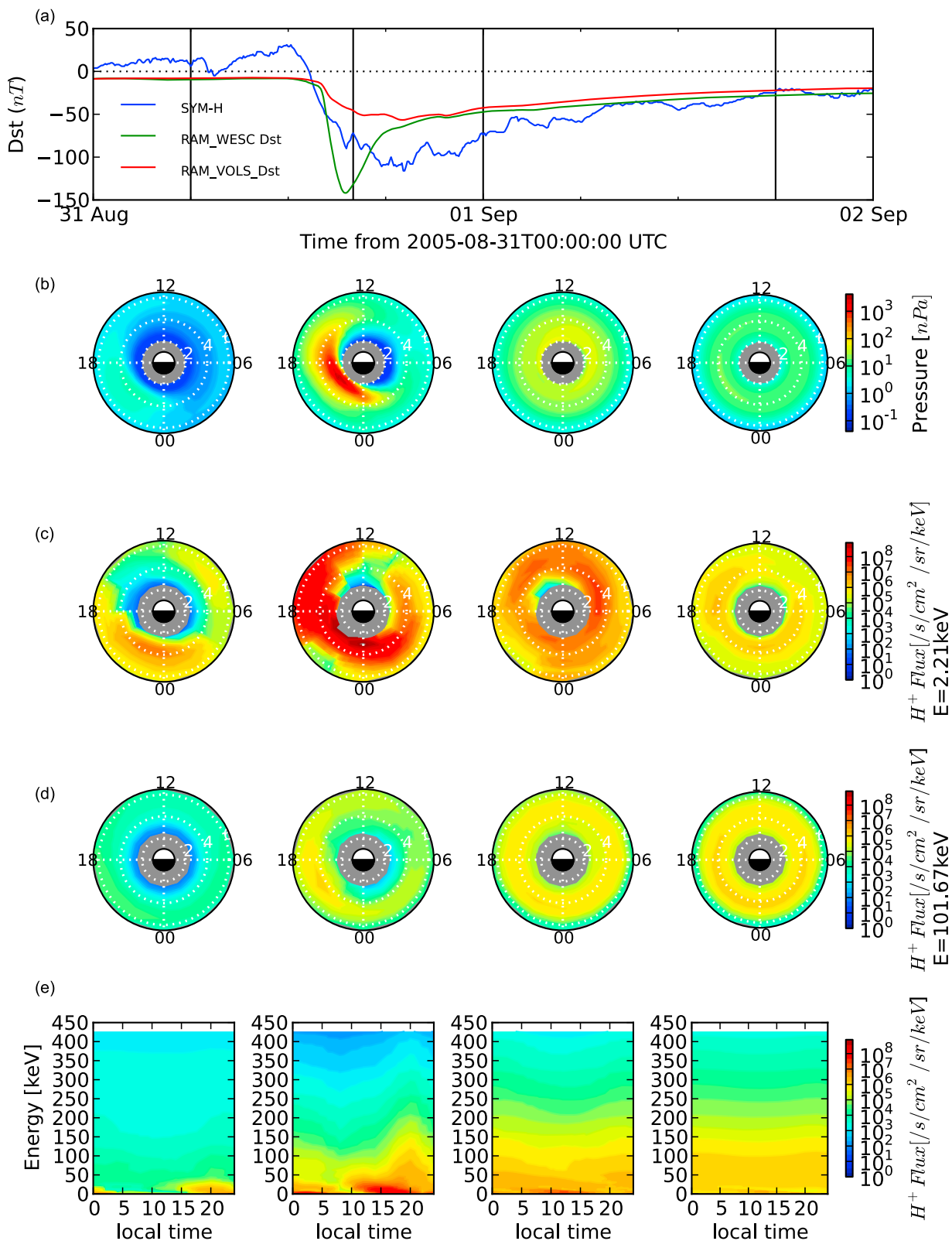


Figure 9. Simulation results for the storm event 31 August 2005. (a) The observed SYM-H index (blue) and the SYM-H index calculated from RAM-SCB model with the Weimer electric field along SCB field lines (WESC, green) and the Volland-Stern electric field (VOLS, red). The remaining plots represent simulation results using the Weimer electric field at four snapshots (time marked by vertical lines): (b) total pressure, (c) H^+ flux at the energy level of ~ 2 keV, (d) H^+ flux at a higher energy level ~ 100 keV, and (e) energy - LT (local time) contour plots of H^+ flux at $4.0 R_E$.

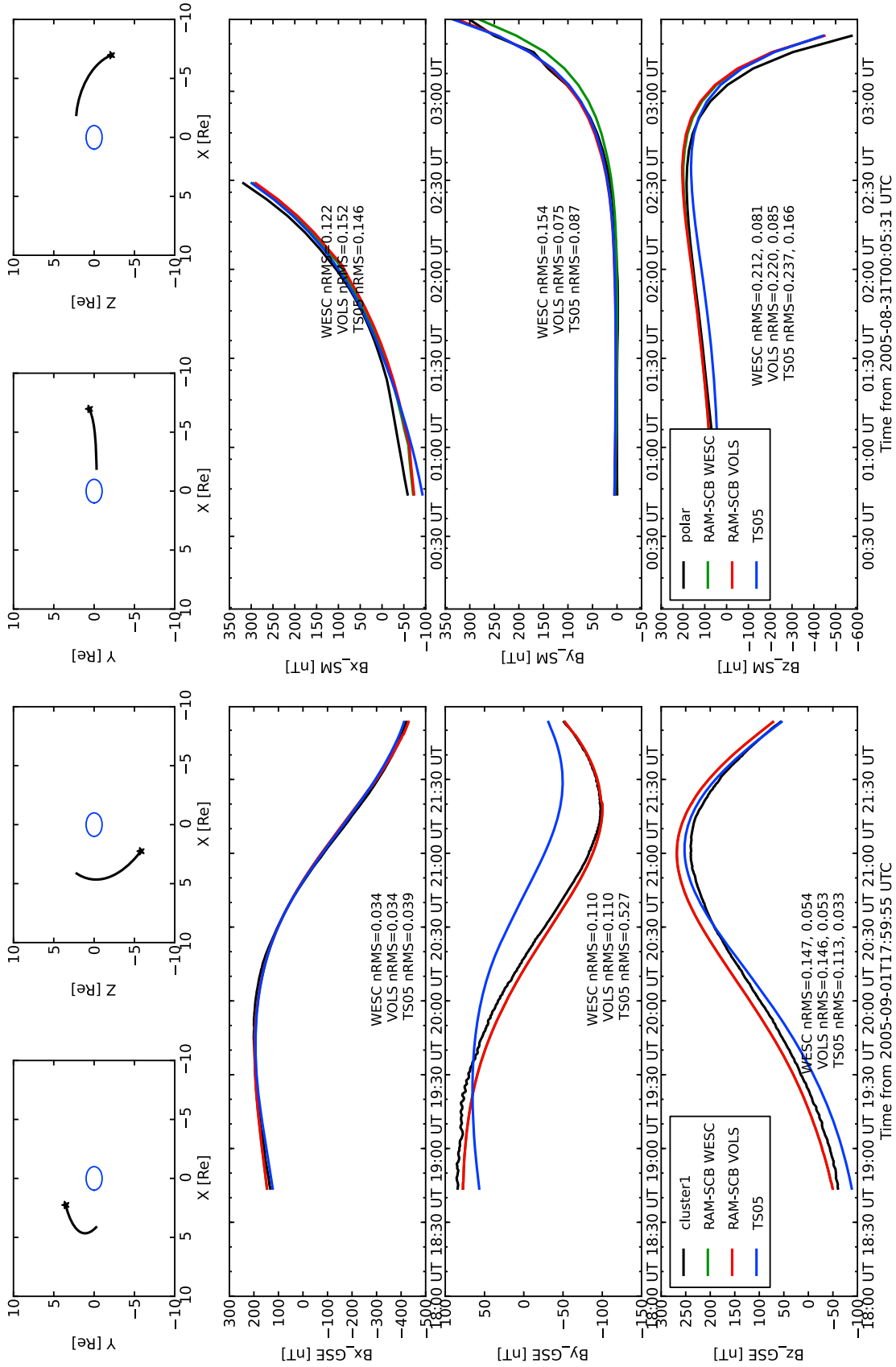
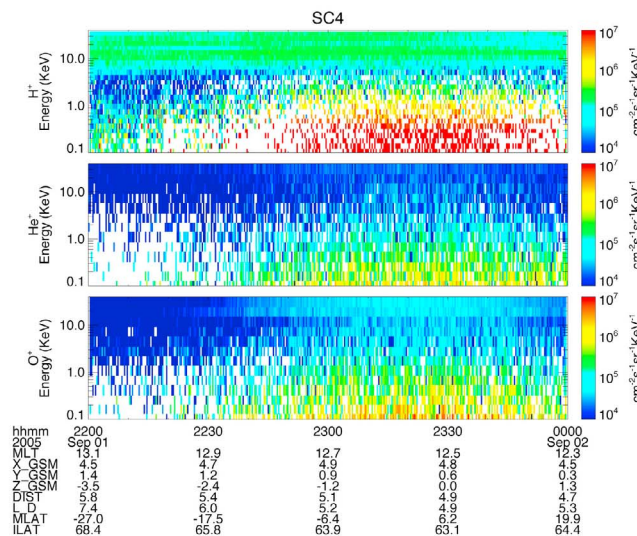
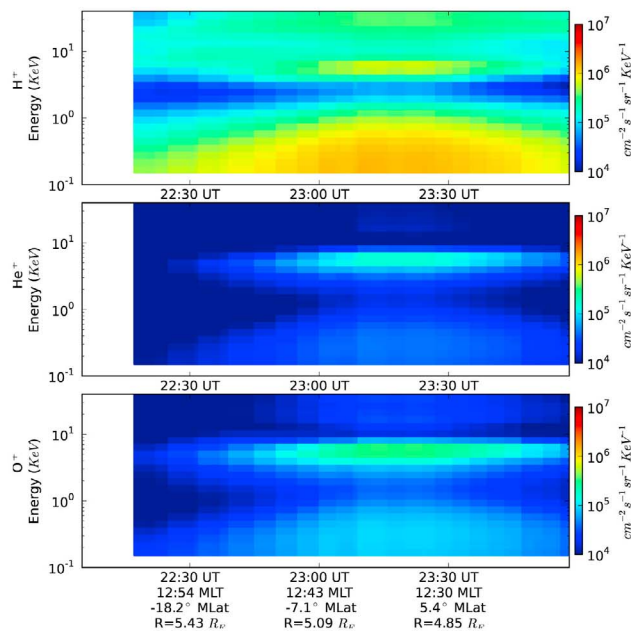


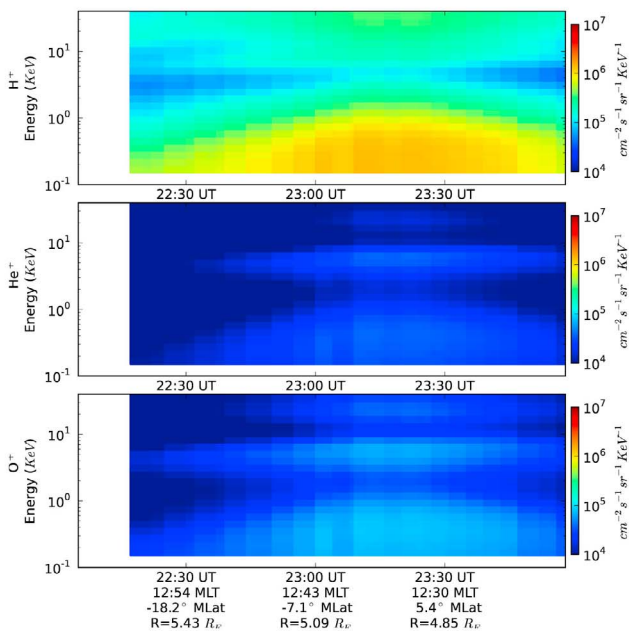
Figure 10. The magnetic field computed by RAM-SCB model using the Weimer electric field driving (WESC, green) and the Volland-Stern electric field driving (VOLS, red) for storm event 31 August 2005. The in situ observation (black line) and the field obtained from the Tsyanenko 05 storm model (blue line) are illustrated for comparison. Left plots show magnetic field along a Cluster trajectory, and right plots show magnetic field along a Polar trajectory. Note that the green and red lines are nearly overlapped in most of the plots. The shown trajectories are inside the model domain. The numerical values are the normalized RMS errors for each field component and magnitude (bottom right plot), measuring the agreement between the model and observation.



(a) Cluster/CODIF observation



(b) RAM-SCB with Weimer01



(c) RAM-SCB with Volland-Stern

Figure 11. Ion flux spectrograms from (a) Cluster/CODIF measurement, (b) RAM-SCB simulation with the Weimer electric field driving, and (c) RAM-SCB simulation with the Volland-Stern electric field driving during the recovery phase of storm 31 August 2005 (time starts from 1 September 2005, 22:00 UT in the plots). The flux is pitch angle averaged.

electric field in the model can play a role in enhancing the ion flux on the dawn side, leading to a better agreement between the model results and the observations.

5.2. Magnetic Storm Event: 31 August 2005

[27] The second magnetic storm event has a minimum SYM-H of -100 nT and a long recovery phase. Figure 9 shows the observed SYM-H index (blue) and modeled SYM-H index using the Weimer model (green) and Volland-

Stern model (red). Again, the modeled SYM-H index using Volland-Stern is much smaller than the observed index, indicating a less intense ring current, while using the Weimer model, the SYM-H index agrees better with the data, although it tends to decrease more sharply to the minimum and recover faster. Four snapshots (marked by the vertical lines in the SYM-H plot) are chosen throughout the storm time in the simulation using the Weimer model: quiet time, main phase, early recovery phase, and late recovery phase. A

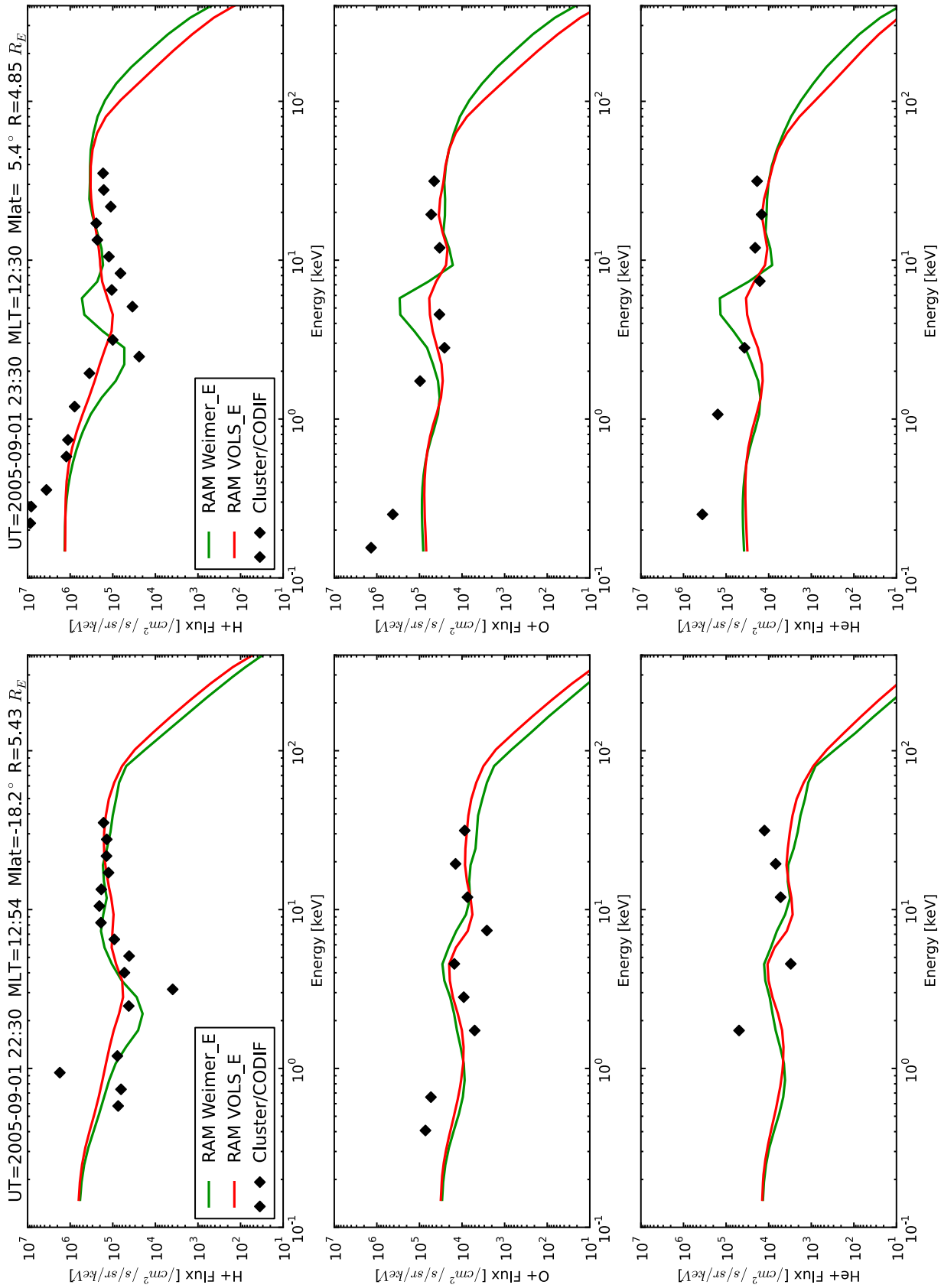


Figure 12. Ion (H^+ , O^+ , He^+) differential flux as a function of energy observed by Cluster/CODIF (diamond) and produced by the model using either Weimer01 (green) or Volland-Stern (red) electric field driving at two different times during the recovery phase of the storm 31 August 2005. The flux is pitch angle averaged.

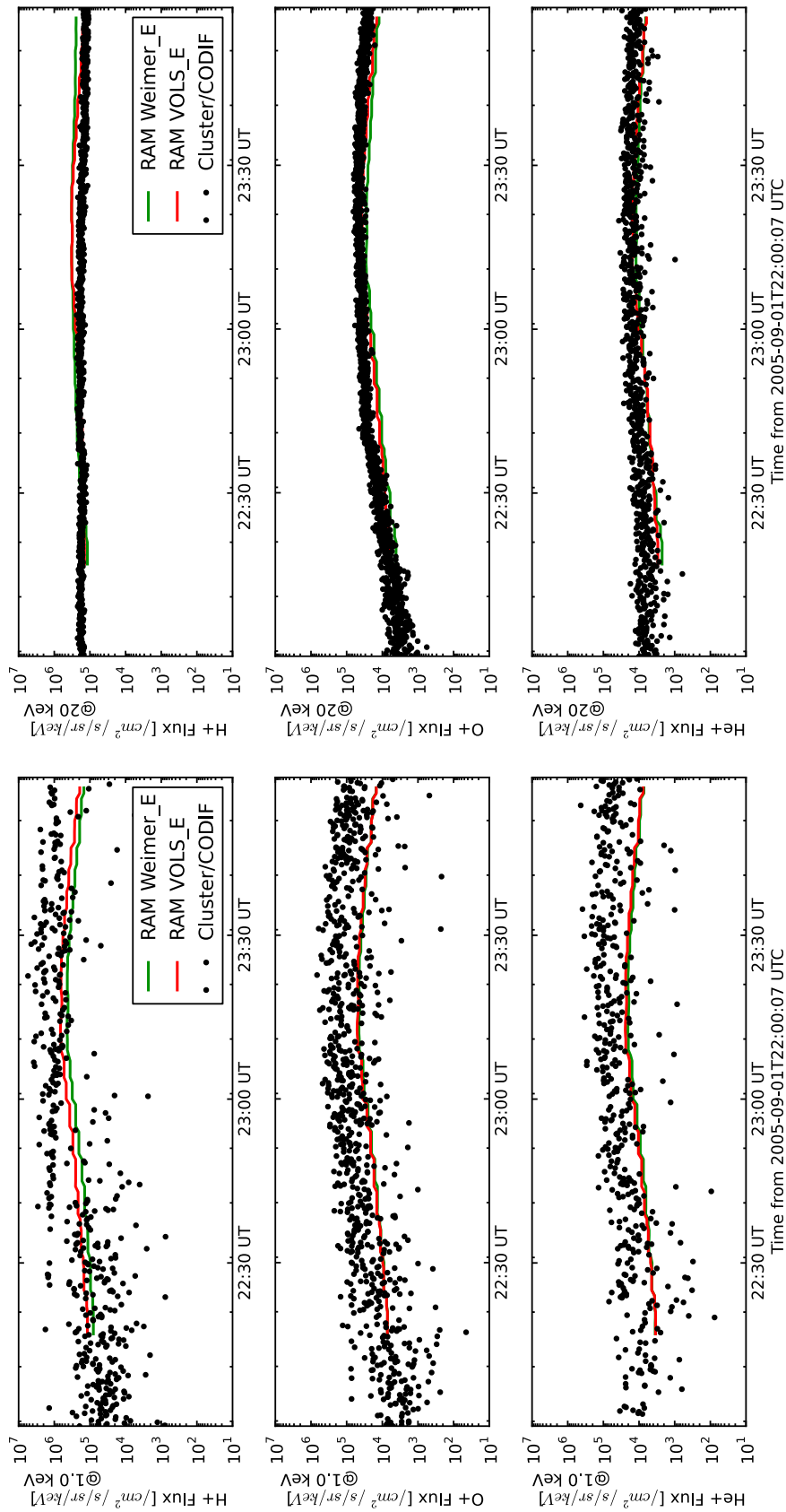


Figure 13. Ion (H^+ , O^+ , He^+) differential flux along the Cluster trajectory observed by Cluster/CODIF (black dots) and produced by the model using either Weimer01 (green) or Volland-Stern (red) electric field driving for two different energy levels: (left) 1 keV and (right) 20 keV, in the storm event 31 August 2005. The flux is pitch angle averaged.

strong partial ring current (Figure 9b) is developed in the main phase on the midnight-dusk sector, and quickly becomes symmetric and gradually fades away. The low energy (~ 2 keV) H^+ flux (Figure 9c) is significantly enhanced at most of the local times during the main phase. The plasma moves westward and part of it leaves the simulation domain from the dayside boundary. The high energy (~ 100 keV) flux (Figure 9d) however is much less intense and no particles seem to leave the boundary as they are mostly trapped by the magnetic field.

5.2.1. Magnetic Field Comparison

[28] The modeled magnetic field is also compared with observations from Cluster and Polar spacecraft. When these satellites orbit inside the model domain, the Cluster satellite is in the dayside magnetosphere toward northern hemisphere during the recovery phase, and the Polar spacecraft is moving toward the Earth on the midnight meridian in the pre-storm time. Both comparisons (Figure 10) indicate good agreements in the magnetospheric field configuration, with most of the normalized RMS errors less than 0.2 for both electric field drivings, implying again that the model can relatively well reproduce the magnetic field within the inner magnetosphere. When compared with the TS05 magnetic fields, the RAM-SCB reproduces better magnetic fields in most of the components.

5.2.2. Differential Ion Flux Comparison

[29] Figure 11 shows pitch angle averaged flux spectrograms from both the Cluster/CODIF observation and RAM-SCB simulations using both Weimer01 and Volland-Stern electric field models. This comparison is carried out when the satellite is flying in the dayside magnetosphere and during the recovery phase. The modeled H^+ flux spectrogram shows a gap region from 1.5 to 3.5 keV using the Weimer electric field model but this spectral gap region is smaller and less intense when using the Volland-Stern electric model. Such a region is consistent with the data. The simulated O^+ flux using either electric field driving is enhanced around 5 keV energy, in different magnitude though, but the instrument hardly detects such an energized band.

[30] The flux as a function of energy at individual times is displayed in Figure 12. When the satellite is near the local time of 13:00, magnetic latitude of -18° , and $5.5 R_E$ away from the Earth (Figure 12, left), the comparison between the data and model with either electric potential model indicates good agreement for both H^+ and O^+ fluxes, while there are very limited He^+ data points to verify the model results. At another time and location near the dayside equator (Figure 12, right), the flux with Weimer model shows a peak near 5 keV, larger than that using the Volland-Stern model. The latter however matches better the observations. The fluxes along the trajectory (Figure 13) at energy level of 1.0 keV (Figure 13, left) fall into the noisy range of the observations, while at a higher energy level (20 keV) the model reproduces well the flux magnitude for all ions (Figure 13, right). Results with the Volland-Stern and Weimer electric field models along this satellite trajectory show no remarkable difference.

6. Summary and Conclusion

[31] This study carried out the validation work of the magnetically self-consistent inner magnetosphere model

RAM-SCB using in situ satellite measurements, including the magnetic field from Cluster and Polar spacecraft, ion differential flux from Cluster/CODIF sensor, and the ground-based magnetic perturbation SYM-H index. The magnetic field in the model is solved in Euler potential coordinates and needs to be interpolated into the Cartesian coordinate system using k-d tree and nearest neighbor interpolation method. The model computes magnetic fields in good agreement with in situ observations and generally performs better in reproducing the B_z component than the empirical TS05 model, suggesting the high reliability of the model in representing the inner magnetospheric configuration and in further applications such as drift shell tracing for the radiation belt community. However, the modeled ion differential flux using different electric field drivings reveals different scenarios. While the low energy flux is generally underestimated using either the Weimer or Volland-Stern electric potential model at dawn sector, the model performance of the moderate and high energy flux strongly depends on electric field strength, local time, and storm activity level. The model utilizing the Weimer model generally captures the SYM-H index profile, implying that the kinetic model with the self-consistently coupled magnetic field is able to represent the ring current dynamics. However, using the Volland-Stern electric field model, the ring current is not as intensified. Future work of implementing a self-consistent electric field can hopefully improve the model capability of reproducing the measurements.

[32] **Acknowledgments.** We greatly thank Reiner Friedel and Steve Morley for providing us with the ion flux from LANL satellite measurements and Malcolm Sambridge from the Australian National University for providing us with the 3-D source code for Delaunay triangulation and natural neighbor interpolation. This work was conducted under the auspices of the U.S. Department of Energy, with support from the Los Alamos National Laboratory Directed Research and Development program, NSF grant ATM-0902941, and NASA grants NNNH09AL061 and NNNH11AR131.

[33] Masaki Fujimoto thanks the reviewers for their assistance in evaluating this paper.

References

- Balogh, A., et al. (2001), The Cluster Magnetic Field Investigation: Overview of in-flight performance and initial results, *Ann. Geophys.*, *19*, 1207–1217, doi:10.5194/angeo-19-1207-2001.
- Bentley, J. L. (1980), Multidimensional divide-and-conquer, *Commun. ACM*, *23*, 214–229, doi:http://doi.acm.org/10.1145/358841.358850.
- Brandt, P., S. Ohtani, D. G. Mitchell, M.-C. Fok, E. C. Roelof, and R. Demajistre (2002), Global ENA observations of the storm mainphase ring current: Implications for skewed electric fields in the inner magnetosphere, *Geophys. Res. Lett.*, *29*(20), 1954, doi:10.1029/2002GL015160.
- Dessler, A. J., and E. N. Parker (1959), Hydromagnetic theory of geomagnetic storms, *J. Geophys. Res.*, *64*, 2239–2252, doi:10.1029/JZ064i012p02239.
- Fok, M.-C., R. A. Wolf, R. W. Spiro, and T. E. Moore (2001), Comprehensive computational model of Earth's ring current, *J. Geophys. Res.*, *106*, 8417–8424, doi:10.1029/2000JA000235.
- Fok, M.-C., N. Buzulukova, S.-H. Chen, P. W. Valek, J. Goldstein, and D. J. McComas (2010), Simulation and TWINS observations of the 22 July 2009 storm, *J. Geophys. Res.*, *115*, A12231, doi:10.1029/2010JA015443.
- Jordanova, V. K., J. U. Kozyra, G. V. Khazanov, A. F. Nagy, C. E. Rasmussen, and M.-C. Fok (1994), A bounce-averaged kinetic model of the ring current ion population, *Geophys. Res. Lett.*, *21*, 2785–2788, doi:10.1029/94GL02695.
- Jordanova, V. K., L. M. Kistler, J. U. Kozyra, G. V. Khazanov, and A. F. Nagy (1996), Collisional losses of ring current ions, *J. Geophys. Res.*, *101*, 111–126, doi:10.1029/95JA02000.
- Jordanova, V. K., J. U. Kozyra, A. F. Nagy, and G. V. Khazanov (1997), Kinetic model of the ring current–atmosphere interactions, *J. Geophys. Res.*, *102*, 14,279–14,292, doi:10.1029/96JA03699.

- Jordanova, V. K., Y. S. Miyoshi, S. Zaharia, M. F. Thomsen, G. D. Reeves, D. S. Evans, C. G. Mouikis, and J. F. Fennell (2006), Kinetic simulations of ring current evolution during the Geospace Environment Modeling challenge events, *J. Geophys. Res.*, *111*, A11S10, doi:10.1029/2006JA011644.
- Jordanova, V. K., S. Zaharia, and D. T. Welling (2010), Comparative study of ring current development using empirical, dipolar, and self-consistent magnetic field simulations, *J. Geophys. Res.*, *115*, A00J11, doi:10.1029/2010JA015671.
- Lemon, C., R. A. Wolf, T. W. Hill, S. Sazykin, R. W. Spiro, F. R. Toffoletto, J. Birn, and M. Hesse (2004), Magnetic storm ring current injection modeled with the Rice convection model and a self-consistent magnetic field, *Geophys. Res. Lett.*, *31*, L21801, doi:10.1029/2004GL020914.
- Liemohn, M. W. (2003), Yet another caveat to using the Dessler-Parker-Sckopke relation, *J. Geophys. Res.*, *108*(A6), 1251, doi:10.1029/2003JA009839.
- Lyons, L. R., R. M. Thorne, and C. F. Kennel (1972), Pitch-angle diffusion of radiation belt electrons within the plasmasphere, *J. Geophys. Res.*, *77*, 3455–3474, doi:10.1029/JA077i019p03455.
- Maynard, N. C., and A. J. Chen (1975), Isolated cold plasma regions: Observations and their relation to possible production mechanisms, *J. Geophys. Res.*, *80*, 1009–1013, doi:10.1029/JA080i007p01009.
- Millan, R. M., R. P. Lin, D. M. Smith, K. R. Lorentzen, and M. P. McCarthy (2002), X-ray observations of MeV electron precipitation with a balloon-borne germanium spectrometer, *Geophys. Res. Lett.*, *29*(24), 2194, doi:10.1029/2002GL015922.
- Reeves, G. D., K. L. McAdams, R. H. W. Friedel, and T. P. O'Brien (2003), Acceleration and loss of relativistic electrons during geomagnetic storms, *Geophys. Res. Lett.*, *30*(10), 1529, doi:10.1029/2002GL016513.
- Rème, H., et al. (2001), First multispacecraft ion measurements in and near the Earth's magnetosphere with the identical Cluster ion spectrometry (CIS) experiment, *Ann. Geophys.*, *19*, 1303–1354, doi:10.5194/angeo-19-1303-2001.
- Roederer, J. G. (1970), *Dynamics of Geomagnetically Trapped Radiation: Physics and Chemistry in Space*, Springer, Berlin.
- Russell, C. T., R. C. Snare, J. D. Means, D. Pierce, D. Dearborn, M. Larson, G. Barr, and G. Le (1995), The GGS/POLAR magnetic fields investigation, *Space Sci. Rev.*, *71*, 563–582, doi:10.1007/BF00751341.
- Sckopke, N. (1966), A general relation between the energy of trapped particles and the disturbance field near the Earth, *J. Geophys. Res.*, *71*, 3125–3130, doi:10.1029/JZ071i013p03125.
- Sibson, R. (1981), A brief description of natural neighbor interpolation, in *Interpreting Multivariate Data*, chap. 2, pp. 21–36, John Wiley, Chichester, U. K.
- Stern, D. P. (1975), The motion of a proton in the equatorial magnetosphere, *J. Geophys. Res.*, *80*, 595–599, doi:10.1029/JA080i004p00595.
- Toffoletto, F., S. Sazykin, R. Spiro, and R. Wolf (2003), Inner magnetospheric modeling with the Rice convection model, *Space Sci. Rev.*, *107*, 175–196, doi:10.1023/A:1025532008047.
- Tsyganenko, N. A. (1989), A magnetospheric magnetic field model with a warped tail current sheet, *Planet. Space Sci.*, *37*, 5–20, doi:10.1016/0032-0633(89)90066-4.
- Tsyganenko, N. A., and M. I. Sitnov (2005), Modeling the dynamics of the inner magnetosphere during strong geomagnetic storms, *J. Geophys. Res.*, *110*, A03208, doi:10.1029/2004JA010798.
- Vallat, C., et al. (2007), Ion multi-nose structures observed by Cluster in the inner magnetosphere, *Ann. Geophys.*, *25*, 171–190, doi:10.5194/angeo-25-171-2007.
- Volland, H. (1973), A semiempirical model of large-scale magnetospheric electric fields, *J. Geophys. Res.*, *78*, 171–180, doi:10.1029/JA078i001p00171.
- Weimer, D. R. (2001), An improved model of ionospheric electric potentials including substorm perturbations and application to the Geospace Environment Modeling November 24, 1996, event, *J. Geophys. Res.*, *106*, 407–416, doi:10.1029/2000JA000604.
- Wolf, R. A. (1983), The quasi-static (slow-flow) region of the magnetosphere, in *Solar Terrestrial Physics*, edited by R. L. Carovillano and J. M. Forbes, pp. 303–368, D. Reidel, Hingham, Mass.
- Yang, J., F. R. Toffoletto, R. A. Wolf, and S. Sazykin (2011), RCM-E simulation of ion acceleration during an idealized plasma sheet bubble injection, *J. Geophys. Res.*, *116*, A05207, doi:10.1029/2010JA016346.
- Young, D. T., H. Balsiger, and J. Geiss (1982), Correlations of magnetospheric ion composition with geomagnetic and solar activity, *J. Geophys. Res.*, *87*, 9077–9096, doi:10.1029/JA087iA11p09077.
- Zaharia, S. (2008), Improved Euler potential method for three-dimensional magnetospheric equilibrium, *J. Geophys. Res.*, *113*, A08221, doi:10.1029/2008JA013325.
- Zaharia, S., C. Cheng, and K. Maezawa (2004), 3-D force-balanced magnetospheric configurations, *Ann. Geophys.*, *22*, 251–265, doi:10.5194/angeo-22-251-2004.
- Zaharia, S., V. K. Jordanova, M. F. Thomsen, and G. D. Reeves (2006), Self-consistent modeling of magnetic fields and plasmas in the inner magnetosphere: Application to a geomagnetic storm, *J. Geophys. Res.*, *111*, A11S14, doi:10.1029/2006JA011619.

V. Jordanova, J. Koller, Y. Yu, and S. Zaharia, Space Science and Application, ISR-1, Los Alamos National Laboratory, Los Alamos, NM 87545, USA. (vania@lanl.gov; jkoller@lanl.gov; yiqun@lanl.gov; szaharia@lanl.gov)

L. M. Kistler and J. Zhang, Space Science Center, University of New Hampshire, Durham, NH 03824, USA. (lynn.kistler@unh.edu; jichun.zhang@unh.edu)